

# Numerical Simulation of Bolide Entry with Ground Footprint Prediction

Michael J. Aftosmis\*

*NASA Ames, Moffett Field, CA*

Marian Nemec†

*Science & Tech. Corp., Moffett Field, CA*

Donovan L. Mathias‡

*NASA Ames, Moffett Field, CA*

Marsha J. Berger§

*NYU, 251 Mercer St., NY, NY*

As they decelerate through the atmosphere, meteors transfer mass, momentum and energy into the surrounding air at tremendous rates. The entry of such bolides produces strong blast waves that can propagate hundreds of kilometers and cause substantial terrestrial damage even when no ground impact occurs. We develop a new technique for meteoroid airburst modeling based upon conservation analysis for the deposition of mass, momentum and energy. These sources are then used to drive simulations of blast propagation using a fully-conservative, finite-volume solver on a multilevel Cartesian mesh. We examine the ability of this method to accurately propagate the blast over hundreds of kilometers of terrain. Initial verification of the method is presented through the canonical problem of a spherical charge. A detailed reconstruction of the 2013 Chelyabinsk meteor provides additional validation. These simulations show very good prediction of the surface overpressure and blast arrival times throughout the ground footprint. Further investigations examine the impact of simplifications to the modeling on both accuracy and computational efficiency using a line-source blast model and a static spherical charge. Both approaches are shown to be useful simplifications and limitations on their use are discussed.

*Keywords:* asteroid, atmospheric entry, blast propagation, meteor, Cartesian, Cart3D

## I. Introduction

IN mid-February 2013 an asteroid measuring approximately 20 meters in diameter entered the sky over Chelyabinsk Russia. The bolide had a mass of about 12,500 metric tons and vaporized nearly completely above 25 km. Despite its relatively small size, the asteroid carried with it tremendous kinetic energy and released the equivalent of approximately 520 kilotons of TNT (about 30 times more powerful than the Hiroshima atomic bomb) into the atmosphere as it entered and burned up.<sup>1</sup> Over a minute later, trauma from this sudden deposition of energy reached the ground, breaking glass and damaging structures in a region covering more than 20,000 square kilometers.

Government infrasound monitoring records an average of around 27 encounters with objects larger than a meter in diameter annually.<sup>2</sup> Each decade, approximately seven encounters occur that release over 10 kilotons into the atmosphere.<sup>3</sup> Since the population of potentially hazardous objects follows a rough power law, the best current estimates predict encounters with Chelyabinsk-sized objects approximately every 80 years.<sup>4</sup>

In response to this threat, NASA's Near-Earth Object program initiated a new research activity in October of 2014, focused on quantifying the risk associated with potentially hazardous meteors and asteroids.<sup>5</sup> This program is structured around four thrusts: (1) characterization and composition, (2) entry/break-up physics, (3) atmospheric propagation and impact effects, and (4) physics-based risk assessment. This paper targets the third of these tasks, namely simulation and modeling for propagation of the airburst through the atmosphere and estimation of its effects at ground level. Clearly this element is closely connected to both

\**michael.aftosmis@nasa.gov*, Computational Aerosciences Branch, Associate Fellow AIAA.

†*marian.nemec@nasa.gov*, Applied Modeling and Simulation Branch, Senior Member AIAA.

‡*donovan.mathias@nasa.gov*, Engineering Risk Assessment Team, Senior Member AIAA.

§*berger@cims.nyu.edu*, Courant Institute, NYU, Senior Member AIAA.

entry physics and risk assessment. In a nutshell, atmospheric propagation takes inputs from entry modeling (task 2) and computes the footprint, on land or water, that drives risk assessment (task 4).

From a simulation and modeling standpoint, entry is typically modeled with highly detailed multi-physics simulations done in the frame of the asteroid as it enters,<sup>6</sup> while atmospheric propagation is usually done in the Eulerian frame of a fixed observer on the ground using energy-deposition as input. The ground or water effects may then be assessed using either analytic models or through correlation of the energy release with static nuclear detonations.<sup>7-9</sup> More detailed analysis has also been performed using numerical simulation of the atmospheric blast propagation using various hydrocodes.<sup>1,3,6,10,11</sup> Such simulations are often driven either by triggering breakup of a known object or by an estimate of the energy deposition profile, which can be generated for specific bolide entries through observation of the light curve<sup>1</sup> or infrasound measurements.<sup>3,12</sup>

In this work, we perform the blast propagation using a fully-conservative, finite-volume scheme on a multilevel Cartesian mesh. Since we seek to drive risk analyses, energy deposition profiles are a useful starting point because they capture the effects of variables like strength, bulk density, fragmentation and entry conditions. These variables can drive parametric studies to understand sensitivities of the ground footprint to characteristics of the entry. This approach also provides the flexibility to drive propagation simulations using outputs from our physics-based entry modeling work, analytic or PDE-based models,<sup>7,8,13-15</sup> observed light curve data, or infrasound measurements.

Using conservation arguments, the analysis section of this paper takes energy deposition as input and derives time-dependent source terms that conserve mass, momentum and energy of the entire system. Numerical results include a validation study using a spherical blast model at relevant conditions. Further validation comes from a detailed reconstruction of the Chelyabinsk superbolide, including comparisons with observational data collected by the Chelyabinsk Airburst Consortium. These data and supporting simulations examine both ground overpressure and blast arrival time using ground damage reports and time-synced video. The goal of this work is to develop a simulation capability that can be parametrically driven to assess the sensitivity of the ground footprint to various parameters characterizing the meteoroid entry. This is clearly a computationally intensive process. We examine at the potential for common simplifications of the meteor entry problem to reduce computational expense and evaluate their impact on the ground footprint predictions that drive risk assessment.

## II. Governing Equations and Numerical Method

### A. Governing Equations

Over the large distances relevant to the entry of meteors and asteroids into the Earth's atmosphere from space, gravitational forces and buoyancy are the main drivers of fluid motion. To account for this, we consider the governing equations for an inviscid, compressible, calorically perfect, heavy gas. This system can be written in strong conservation-law form over a fluid element  $\Omega$  with closed boundary  $\partial\Omega$  and outward facing normal  $\hat{n}$ .

$$\frac{d}{dt} \int_{\Omega} U dV + \oint_{\partial\Omega} (\mathbf{F} \cdot \hat{n}) dS = \int_{\Omega} S dV \quad (1)$$

Where  $U$  is the state vector of conserved variables

$$U = (\rho, \rho u, \rho v, \rho w, \rho E)^T \quad (2)$$

with density,  $\rho$ , Cartesian velocity components  $u, v, w$  and internal energy,  $E$ . The flux-density tensor,  $\mathbf{F}$ , describes the flow of mass, momentum and energy through the fluid element:

$$\mathbf{F} = \begin{pmatrix} \rho u & \rho v & \rho w \\ \rho u^2 + p & \rho uv & \rho uw \\ \rho uv & \rho v^2 + p & \rho vw \\ \rho uw & \rho vw & \rho w^2 + p \\ u(\rho E + p) & v(\rho E + p) & w(\rho E + p) \end{pmatrix} \quad (3)$$

Gravity adds a body force term,  $S$ , that balances the pressure gradient in the momentum equations and

performs work in the energy equation.

$$S = \begin{pmatrix} 0 \\ -\rho g_x \\ -\rho g_y \\ -\rho g_z \\ -\rho(ug_x + vg_y + wg_z) \end{pmatrix} \quad (4)$$

## B. Atmospheric Model

For a stagnant fluid,  $u = v = w = 0$ , with gravity pointing down,  $g = (0, 0, g_z)^T$ , the governing equations reduce to a simple statement of *hydrostatic equilibrium*, where gravitational forces are balanced by a static pressure gradient in the fluid.

$$\frac{\partial p}{\partial z} = -\rho g_z \quad (5)$$

Integrating eq.(5) for a perfect gas at isothermal conditions results in a classic scale height atmosphere model

$$\frac{p(z)}{p_o} = e^{-z/H} \quad (6)$$

where  $H$  is the *scale height* and  $z$  is the geometric altitude. The scale height is usually taken to be in the neighborhood of 7–8 km for engineering approximations of the Earth's atmosphere. At 273 K,  $H$  is 8 km and the mean scale height from sea level to 70 km is about 7.6 km.

Figure 1 compares the pressure and temperature distributions for the 1976 ISO-Standard Atmosphere<sup>16</sup> with those of an isothermal scale height model.<sup>a</sup> While atmospheric pressure varies by over five orders of magnitude, temperature fluctuations in the standard atmosphere are confined to about  $\pm 40$  K in the first 80 km of altitude. Since this is above the height at which most large bolides begin to deposit substantial energy, the isothermal approximation is reasonable for the current analysis. The maximum local deviation occurs at the tropopause (near 10 km) where temperature is at a local minima and the sound speed would be too high by about 6%.

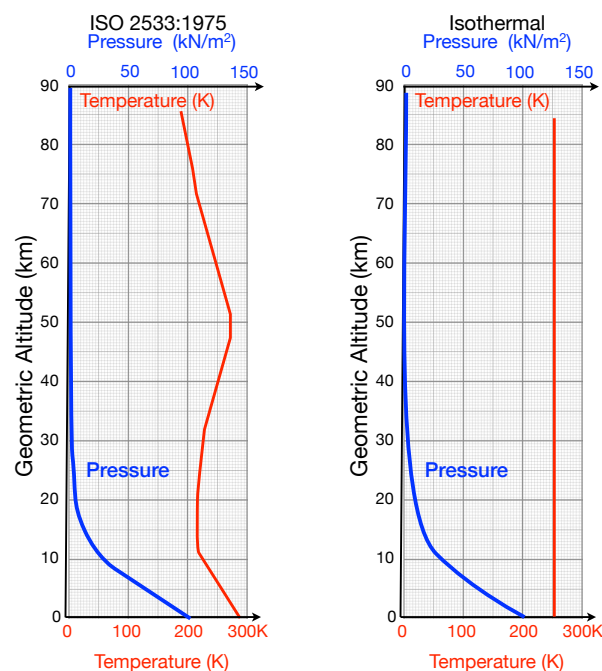


**Figure 1. Comparison of pressure and temperature profiles in the ISO-Standard Atmosphere<sup>16</sup> (left) with an isothermal model (right).**

<sup>a</sup>ISO 2533:1975 is identical to the US Standard Atmosphere below 32 km.

When bolides enter the atmosphere, the rate of energy deposition increases exponentially until reaching a peak value and then tapers off very quickly as fragmentation and deceleration take their toll. The altitude at which peak deposition occurs is known as the *burst height*,  $z_b$ . In this work we establish the scale height in eq.(6) by setting

$$H = \frac{-z_b}{\ln(p_{z_b}/p_o)} \quad (7)$$

and taking the pressure at the burst altitude,  $p_{z_b}$ , and the ground pressure,  $p_o$ , from the standard atmosphere. For a meteor with a burst height of 20 km, this yields a scale height of about 6.86 km, and simultaneously matches ambient pressure at both the ground and the airburst. By choosing the scale height in this way, we ensure that shocks generated near the burst height have the appropriate strength and that ground overpressures are properly calibrated.

The main weakness in the isothermal approximation is a slight skewing of propagation speed, which can impact predictions of the blast arrival time at the ground. From 30 km in the standard atmosphere, a

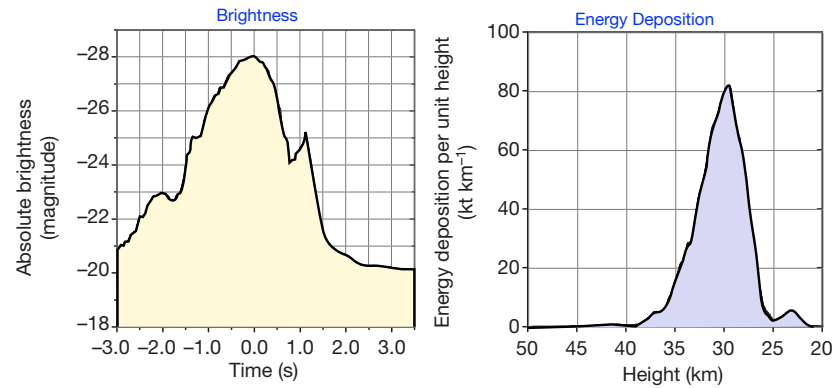


**Figure 2.** Sample observational data from entry of Chelyabinsk meteor, 15 Feb., 2013. (Middle) Light curve reconstruction for absolute brightness.<sup>3</sup> (Right) Energy deposition profile as a function of altitude.<sup>3</sup>

sound wave takes roughly 100 sec to reach the ground. The model used here would under-predict this propagation time by about three seconds. In reality the local atmosphere varies substantially from the standard atmosphere, and propagation is also strongly affected by wind, humidity and other atmospheric phenomena. Such uncertainty makes it hard to reasonably expect predictions of propagation time with significantly better accuracy – especially for impromptu natural events like meteor entry.

### C. Deposition of Mass, Momentum and Energy

During its violent entry, a meteoroid transfers mass, momentum and energy into the surrounding air at tremendous rates. Photographs, light-curve spectra, infrasound recordings and other data are frequently processed to express the net effects of the near-field entry physics in terms of the energy released as functions of both time and altitude. Figure 2 shows a sample of such observational and processed data for the 2013 Chelyabinsk meteor. A snapshot of the entry is shown at the left and the plot at the right shows a reconstruction of the *energy deposition profile* as a function of altitude. Absolute brightness is shown in the middle, and the time of peak brightness corresponds to the peak rate of energy deposition.

This abstraction of the entry physics is useful in modeling, and many entry models produce similar profiles as their primary output.<sup>1, 13–15, 17</sup> In general, energy deposition profiles like these can be produced from observation, hydrocode simulations, engineering models and other sources. These profiles are useful because they capture the effects of variables like strength, bulk density, fragmentation and entry conditions and can be used to drive parametric studies for understanding trends or even to reconstruct specific events.<sup>7, 14</sup>

From the point of view of an Eulerian frame fixed on the ground, this deposition can be modeled as a time-dependent source for the state of the fluid in a control volume surrounding the trajectory of the entering body. To aid in this analysis, Figure 3 shows a tube-like control volume sketched around the trajectory of a body passing through the atmosphere at high speed. Our goal is to derive expressions for time dependent source terms of mass, momentum and energy released into a corridor of known radius,  $r$ , surrounding the trajectory. Although this derivation is essentially a straightforward conservation analysis, we present it in some detail since we have not encountered it in the literature.

Given an energy deposition as a function of height,  $h$ , as shown at the right of Figure 2, the total energy released into the atmosphere is the area under the profile.

$$E_{tot} = \int \frac{dE}{dh} dh + \text{radiation} \quad (8)$$

The net energy released as radiation depends on numerous factors but is typically only around 5–10% of the total. At present, we don't treat radiation

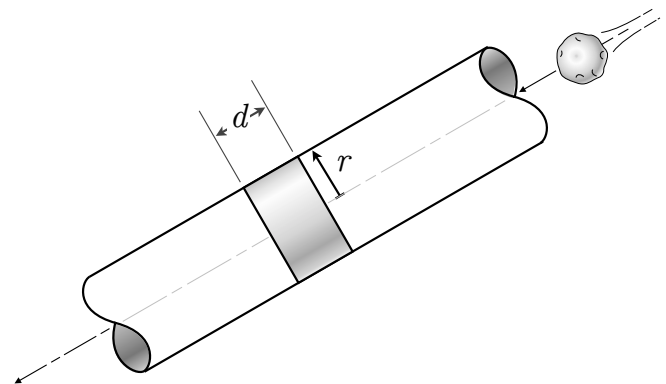


**Figure 3.** Control volume around trajectory of entering body used for converting energy-deposition profile data into time-dependent source terms for fluid state.

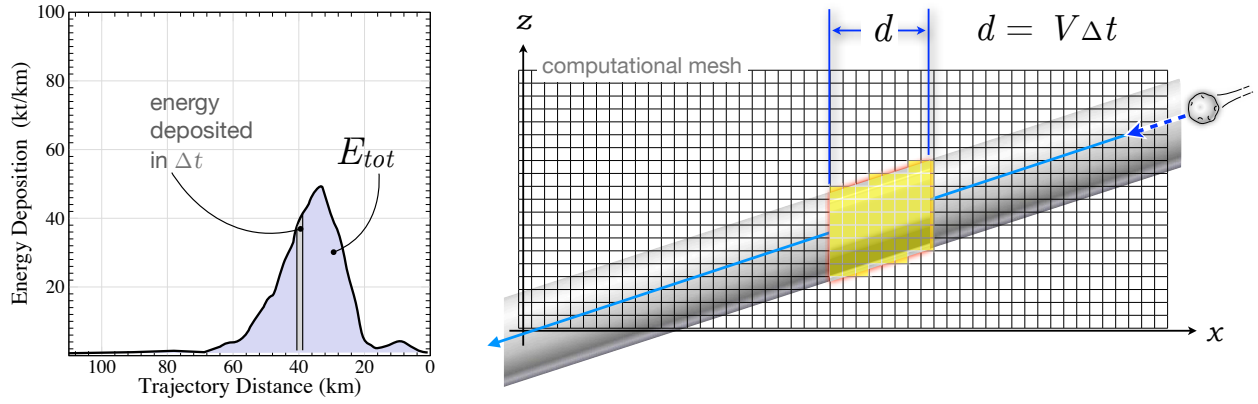


**Figure 4.** Energy released as function of distance along trajectory. This energy is deposited into cells within the computational mesh that fall within the control volume around the flight path at each time step.

explicitly and instead simply deduct an estimate of the total radiative emission from the kinetic energy of the meteoroid in space prior to entry.

With typical entry speeds on the order of 15–50 km/sec,<sup>18</sup> the entire event is over in a few seconds. At these time-scales, gravitational acceleration can only alter the trajectory by a few dozen m/sec after entry interface. With this observation, it is clear that the entry trajectory is essentially a straight line. Thus knowing the entry angle, we can re-express the energy deposition as a function of distance along the trajectory,  $\xi$ .

$$E_{tot} = \int \frac{dE}{d\xi} d\xi \quad (9)$$

Since the trajectory is linear, this transformation is essentially a rescaling of the vertical axis such that the total area under the profile,  $E_{tot}$  remains constant. Over some time  $\Delta t$ , this rescaled profile now determines exactly how much energy gets released into the mesh cells that fall within the control volume set up around the flight path as shown in Figure 4.

An alternative view is that  $E_{tot}$  is the amount of work done by the atmosphere to stop the meteor. This is simply Newton's third law. The ordinate of the energy deposition plot at the left of Figure 4 has units of kilotons of energy deposited per kilometer of trajectory. One kiloton of TNT contains  $4.184 \times 10^{12}$  joules, and joules per kilometer has units of force. Since force  $\times$  distance is work, and aerodynamic drag is the only mechanism for arresting the fragmenting bolide, this plot of energy deposition is actually a record of dimensional drag along the trajectory,  $D(\xi)$ .

$$E_{tot} = \int \frac{dE}{d\xi} d\xi = \int D(\xi) d\xi \quad (10)$$

This almost trivial observation is actually quite powerful, since it now allows us to turn to the problem of mass conservation. In meteor physics, the mass-loss equation for an ablating body is usually written as<sup>12–15, 19</sup>

$$\frac{dM}{dt} = -\sigma C_D S_m \frac{1}{2} \rho_{air} U_m^3 \quad (11)$$

where  $\sigma$  is the ablation coefficient,  $M$  is mass,  $S_m$  is reference area, and  $U_m$  is the body's velocity. Aerodynamic drag is

$$D = C_D S_m q_\infty \quad \text{with} \quad q_\infty = \frac{1}{2} \rho_{air} U_m^2 \quad (12)$$

and so mass loss along the trajectory becomes simply:

$$\frac{dM}{dt} = -\sigma U_m D(\xi) \quad (13)$$

Since  $\frac{dM}{dt} = \frac{dM}{d\xi} \frac{d\xi}{dt} = \frac{dM}{d\xi} U_m$ , we can now relate the total mass deposited to the aerodynamic drag profile.

$$M_{tot} = \int \frac{dM}{d\xi} d\xi = \int -\sigma D(\xi) d\xi \quad (14)$$

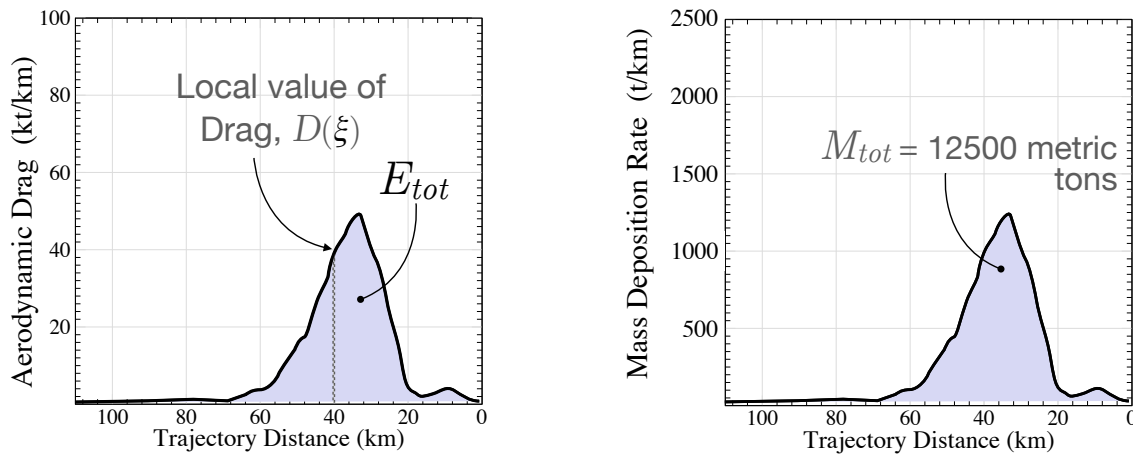


**Figure 5.** Equivalent aerodynamic drag (eq. 10) and mass loss rate (eq. 14) as functions of trajectory distance.  $1 \text{ kt/km} = 4.184 \times 10^9 \text{ N}$ . Mass loss in metric tons per kilometer (t/km) under assumptions of constant ablation coefficient. The total mass deposited is the pre-entry mass minus the mass of surviving fragments.

Under the assumption of a constant ablation coefficient, eq. (14) is simply a local rescaling of the dimensional drag along the trajectory such that the area under the resulting profile is the total mass deposited. For most bolides this is 90-95% of the incoming mass of the meteor. Looking at the terms in this equation, drag is clearly the main driver. The roughly 20 m object that entered above Chelyabinsk experienced about 400,000 pounds of drag at 80 km. This net arresting force grew over 5 orders of magnitude to around 47 billion pounds near peak deposition at 29.5 km.<sup>b</sup> Of course, the velocity also varies as the object decelerates. However, the vast majority of this deceleration doesn't occur until after peak brightness. Hills and Goda<sup>15</sup> illustrate this point by integrating the equations of motion for incoming objects ranging from iron meteoroids to low-density "fluff" over speeds of 12–30 km/sec and show that at peak deposition these objects all still retain 85-90% of their incoming velocity. The ablation coefficient is a simplification of complex physical phenomena, and while in reality it can vary significantly over a trajectory, it is typically assigned a single best fit value.<sup>19</sup> Under these assumptions, Figure 5 shows the variation in aerodynamic drag and mass deposition over the trajectory.

The goal of this entry model is to predict the ground footprint for a given energy deposition profile. There is room to improve this model by incorporating additional physics (for ablation, radiation, etc.) or through direct integration of the meteor equations<sup>13–15</sup> to remove some simplifying assumptions. However, the primary drivers are clearly captured, and it is worthwhile to assess this entry model before attempting to add additional physics.

## D. Numerical Method

Simulations in this work use a solver based on the Cartesian cut-cell approach of [20] in which the governing equations (1)–(4) are discretized on a multilevel Cartesian mesh with embedded boundaries. The mesh consists of regular Cartesian hexahedra everywhere, except for a layer of body-intersecting cut-cells that intersect the geometry at boundaries. Although it consists of nested Cartesian cells, the mesh is represented as an unstructured collection of control volumes making the approach well-suited for solution-adaptive mesh refinement.

The spatial discretization uses a second-order accurate finite-volume method with a weak imposition of boundary conditions. The flux-vector splitting approach of van Leer is used for residual evaluation<sup>21</sup> and monotonicity is controlled through the use of slope limiters in the reconstruction.<sup>22</sup> Time-dependent flow solutions are obtained using a dual-time approach in which an inner Runge–Kutta based multigrid smoother drives a fully implicit outer scheme using second-order backward differencing for unconditional stability. The basic approach follows Jameson<sup>23</sup> although the implementation uses an implicit treatment of the physical time source term within the Runge–Kutta scheme as in [24].

Domain decomposition via space-filling curves permits parallel computation, and the solver has excellent scalability up to several thousand processing cores.<sup>25</sup> This solver has been well validated on scores of internal and external aerodynamic flows over a wide range of speeds.<sup>26</sup> Nevertheless, it has seen much less application to atmospheric flows and rarely has it been used in situations as energetic as those considered in this work.

<sup>b</sup>For altitude see Fig. 2, for magnitude see Fig. 4.

### III. Numerical Investigations

#### A. Strong Spherical Blast

Unlike the classical analyses of Taylor and von Neumann for blasts emanating from a point source,<sup>29,30</sup> analytic solutions do not exist for a spherical charge of finite size. Nevertheless, as a multidimensional counterpart to the standard 1-D shock-tube, the blast from a spherical charge has been well studied both computationally and experimentally, making it a good model problem for validation.<sup>27,28,31</sup> The main goals of this example are to demonstrate the energy deposition, validate the scheme's propagation behavior and verify the stability of the numerics for blasts of realistic magnitude.

We consider the example of an isolated uniform charge with no buoyancy. This simulation was initiated by adding 520 kt of internal energy inside a sphere with a radius of 1 km. Since there are relatively few experimental datasets with relevant levels of energy release, a well-validated 1-D spherical blast model was used for evaluation.<sup>27,28,31</sup> To better mimic the 1-D blast model, buoyancy in the current Cartesian finite-volume scheme was disabled. While fully 3-D, the simulation took advantage of two-fold symmetry and used a domain measuring  $240 \times 120 \times 120$  km. Cartesian cells measuring 62.5 m were used near the initial charge and these were progressively coarsened to around 500 m at a distance of 40 km and to 1 km around 50 km from the blast center. In all, the multilevel Cartesian mesh contained  $\sim 40$  M control volumes.

Figure 6 shows blast evolution through traditional space-time plots of the centerline pressure, in both linear (left) and normalized logarithmic coordinates (right). Results with the numerical method described in § II are shown as color contours, with red indicating overpressure and blue indicating underpressure. These results are compared with the blast front from a 1-D spherical blast model.<sup>27,28</sup> The plot on the left shows  $x-t$  evolution in physical dimensions (km vs. sec) while the logarithmic plot is non-dimensional. The sound speed in dry air at  $20^\circ\text{C}$  (343.59 m/sec) was used to normalize velocity, and time is normalized by the time required for an acoustic wave to propagate one kilometer. The plot on the right shows the blast wave decelerating logarithmically until it asymptotes as an acoustic wave with unit slope in the normalized coordinates as predicted by classical analysis. Detailed comparisons of instantaneous pressure and velocity profiles (not shown) were also conducted against both in-house 1-D blast simulators and 1-D codes available in the literature.<sup>31</sup> Taylor's analysis shows that since a spherical blast is essentially a control volume, the propagation speed is a direct function of the input energy.<sup>29</sup> Consequently, the fully conservative finite volume method used in this work essentially guarantees the correct propagation speed for a given charge strength.

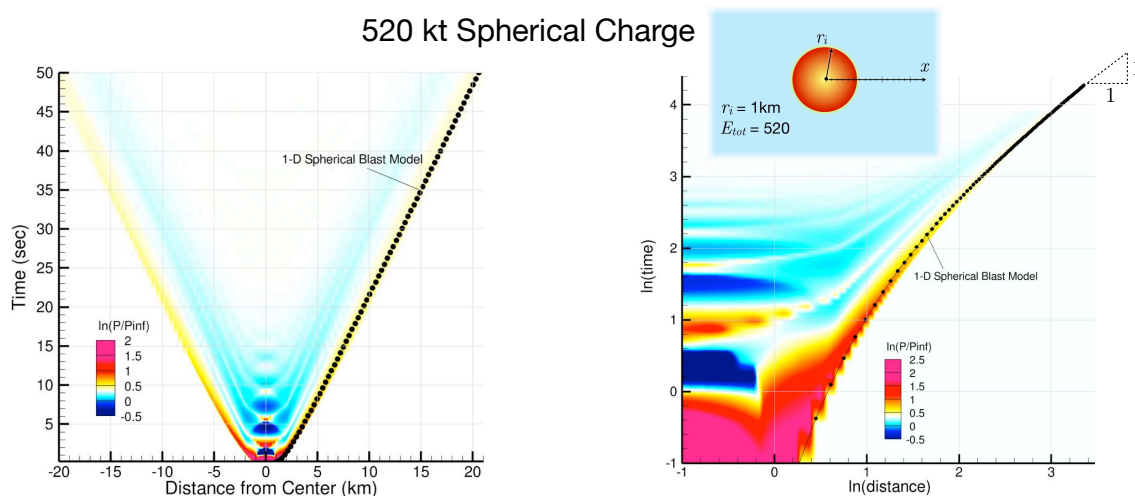


Figure 6. Space-time overpressure plot resulting from evolution of an isolated spherical charge with total energy of 520 kt with no buoyancy. Simulation results compare evolution from the 3-D simulation (contours) with one-dimensional spherical charge model (black symbols).<sup>27,28</sup> Linear scaling (left) logarithmic axes (right).



## B. Chelyabinsk Meteor

### 1. Setup

Despite the damage and injury, the Chelyabinsk meteor of February 2013 provides one of the best validation datasets available in the annals of meteor physics. This superbolide arrived late in the morning commute over a well populated area and reached an absolute magnitude of -28 at peak brightness. Its entry deposited energy equivalent to a magnitude 7.02 earthquake into the atmosphere, breaking windows and collapsing roofs of over 7,300 structures covering a region of more than 20,000 square kilometers.<sup>1,3,32</sup> Both the entry itself and the arrival of the blast wave were captured on hundreds of digital video recorders, making detailed reconstructions of its trajectory and light-curve possible. Field surveys of over 1,600 witnesses yielded a wealth of data documented by the Chelyabinsk Airburst Consortium. Best estimates indicate the meteoroid was 19.6 m in diameter with a mass of  $\sim 12,500,000$  kg.<sup>c</sup> The light curve and infrasound are well correlated for energy deposition, giving a high degree of confidence in the initial conditions.<sup>1,33</sup>

The entry trajectory was inclined  $18^\circ$  with respect to the horizon and peak brightness occurred near the half-energy height at 29.5 km altitude. Figure 2 shows both the brightness as a function of time and energy deposition as a function of altitude from [3]. A total of 520 kt of energy was released to the atmosphere.

In the simulation, the computational domain was 80 km high and extended 256 km both downrange and crossrange along the ground plane. This domain captured almost 110 km of the terminal flight path, extending from an entry interface altitude of 64 km down to 26.6 km after the last major fragmentation. The computational mesh was refined along the trajectory to roughly 20 m spatial resolution and around 80 m resolution on the ground near the region of maximum surface overpressure. In total, the computational mesh contained 92 M cells. Time dependent sources of mass, momentum and energy were deposited into a tube surrounding the trajectory with a radius of 100 m. Thus, the diameter of the tube is a bit less than 1% of the distance from the end of the trajectory to the ground.

### 2. Airburst and Propagation

Figure 7 shows simulation results for the meteor through a sequence of snapshots of local Mach number and local overpressure taken on a vertical plane downrange along the trajectory. Overpressure contours are expressed relative to the local ambient pressure, with white, red and blue indicating ambient, high, and low respectively. The times shown are measured with respect to entry start at 64 km and peak brightness occurs at  $t = 4.2$  sec. The top frame shows the intense cylindrical shock surrounding the trajectory as a result of the high-Mach entry roughly 2.4 seconds after peak brightness. The small ( $\sim 5$  km) nib at the end is associated with a final fragmentation event evident in the energy deposition profile (fig. 5). In the short time since peak brightness, the cylindrical blast wave has already propagated 5–7 km from the trajectory due to the tremendous overpressures at these entry Mach numbers. It is also worth pointing out that at this time scale the contours remain roughly symmetric around the trajectory since buoyancy has not yet had an opportunity to meaningfully accelerate the superheated gas within the shock.

The middle frame in Figure 7 shows the evolution roughly 30 sec later. By this point the shock has weakened and slowed substantially — similar to the deceleration seen in the  $x-t$  plots of the spherical charge example (Fig. 6). Although a factor of ten more time has elapsed since peak brightness, the cylindrical shock has only expanded by about another factor of two beyond the upper picture. The effects of buoyancy are becoming obvious and the structures are becoming notably asymmetric.

The final frame is taken over a minute later, at an elapsed time of 93.7 sec as the blast is running along the ground. At this point the overpressure footprint extends roughly 38 km downrange and about 30 km crossrange. The overpressure plot is especially interesting since the shock reflection off the ground intensifies the overpressures. The color map shows this clearly as these high overpressures (red) sweep the landscape. By this point, buoyancy effects are significant and the flow inside the shock system is highly distorted. Although modified by buoyancy, the cylindrical blast is expanding at just over the sonic velocity and the local propagation speed on the ground simply depends on the geometric intersection of the expanding blast and the ground plane.

<sup>c</sup>Credible estimates of velocity and mass are from 18.5 to 19.3 km/sec and between 12,000 and 13,000 metric tons.<sup>1</sup>



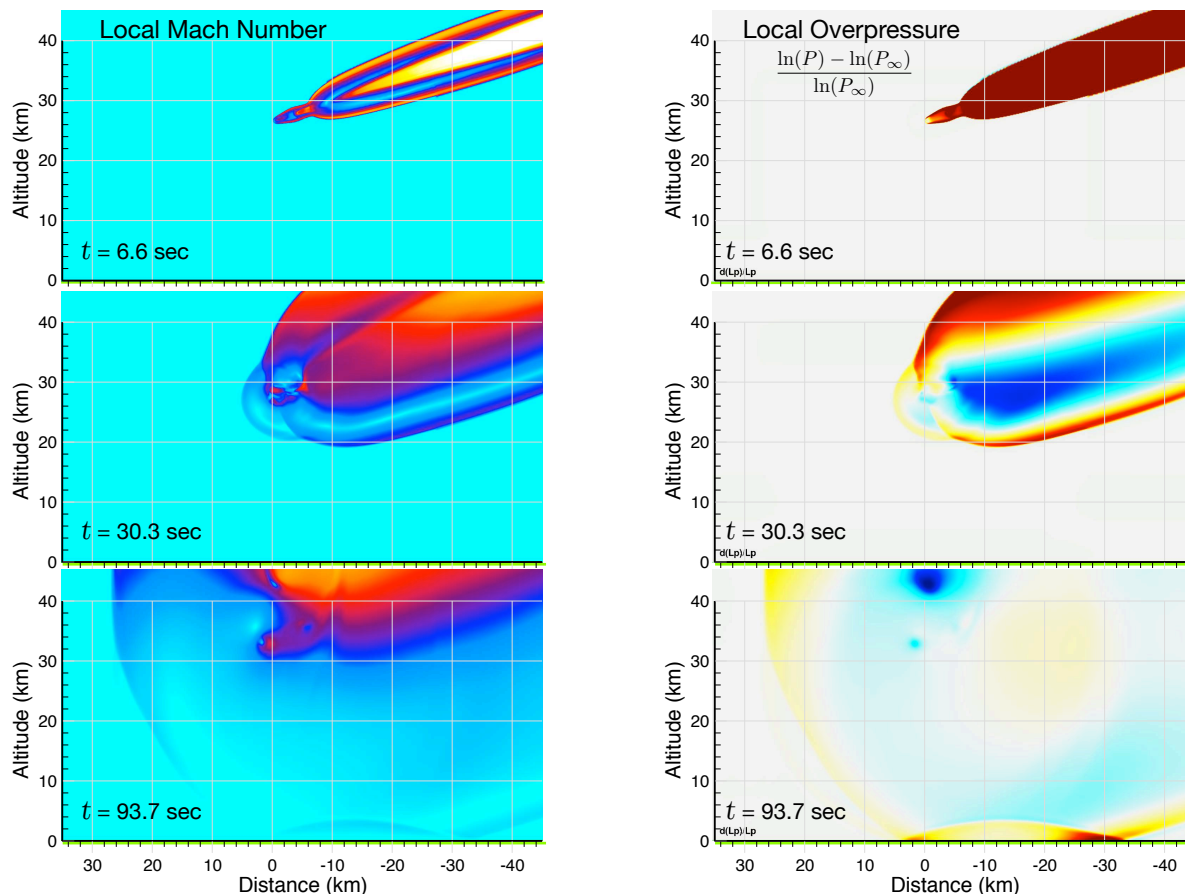


Figure 7. Simulation results for Chelyabinsk meteor using deposition profile from Brown *et al.*<sup>3</sup> Entry angle =  $18^\circ$ , with peak brightness at 29.5 km altitude and  $t = 4.2$  sec. Total energy = 520 kt. Evolution of the entry and propagation is shown via contours of Mach number (left) and local overpressure (right).

### 3. Ground Footprint

Figure 8 shows four views of the ground footprint as the blast propagates through the domain at 160 sec elapsed time. At this point the blast covers an egg-shaped region roughly  $90 \times 110$  km in size. Panels (a) and (b) in Figure 8 show aerial views of the ground footprint through contours of instantaneous pressure and peak recorded overpressure, respectively. The line plot in 8(c) shows instantaneous overpressure at 160 sec along the downrange cut  $AA'$  in percent of ambient sea level pressure. Figure 8(d) shows a similar cut crossrange along  $BB'$ . In this direction, the instantaneous pressure profile is remarkably similar to the classic Friedlander waveform that results from similarity solutions for point source blasts.<sup>29,30</sup> While the long axis of the footprint is in the downrange direction, the highest peak overpressures are at the edges of the crossrange envelope (see Figs. 8a and 8d). The blast can be thought of as a cylindrical shock with a hemispherical endcap. Blast theory for shaped charges predicts that overpressure drops more quickly in the spherically expanding endcap than in the radially expanding cylindrical portion of the shock (which has fewer dimensions in which to expand). This is reflected in the peak overpressure plot in Figure 8(b), where contours of peak overpressure are elongated in the crossrange direction. Essentially the footprint opens like an aperture elongated along the trajectory leaving elliptically shaped contours that are aligned crossrange.

The simulation continued until an elapsed time of over five minutes. At that point, the peak ground overpressures were less than 0.5% of ambient and low enough not to be hazardous. Figure 9 shows the final ground overpressure footprint predicted by this simulation with an overlay of the entry trajectory as seen from above. The origin of the plot on the left is at the end of the simulated trajectory (altitude = 26.6 km). Isobars in both frames have an increment of 1% of ambient pressure (sea level, standard atmosphere). The map at the right shows the predicted ground-footprint overlaid onto glass damage data reported by the Chelyabinsk Airburst Consortium.<sup>1</sup> Red and orange filled circles show broken windows. Statistical correlations in Mannan and Lees<sup>34</sup> for blast-wave data indicate that an overpressure of  $\sim 700$  Pa (0.69%) shatters about 5% of typical unsupported glass windows, while  $\Delta p$  of  $\sim 6\%$  breaks roughly 90%. The

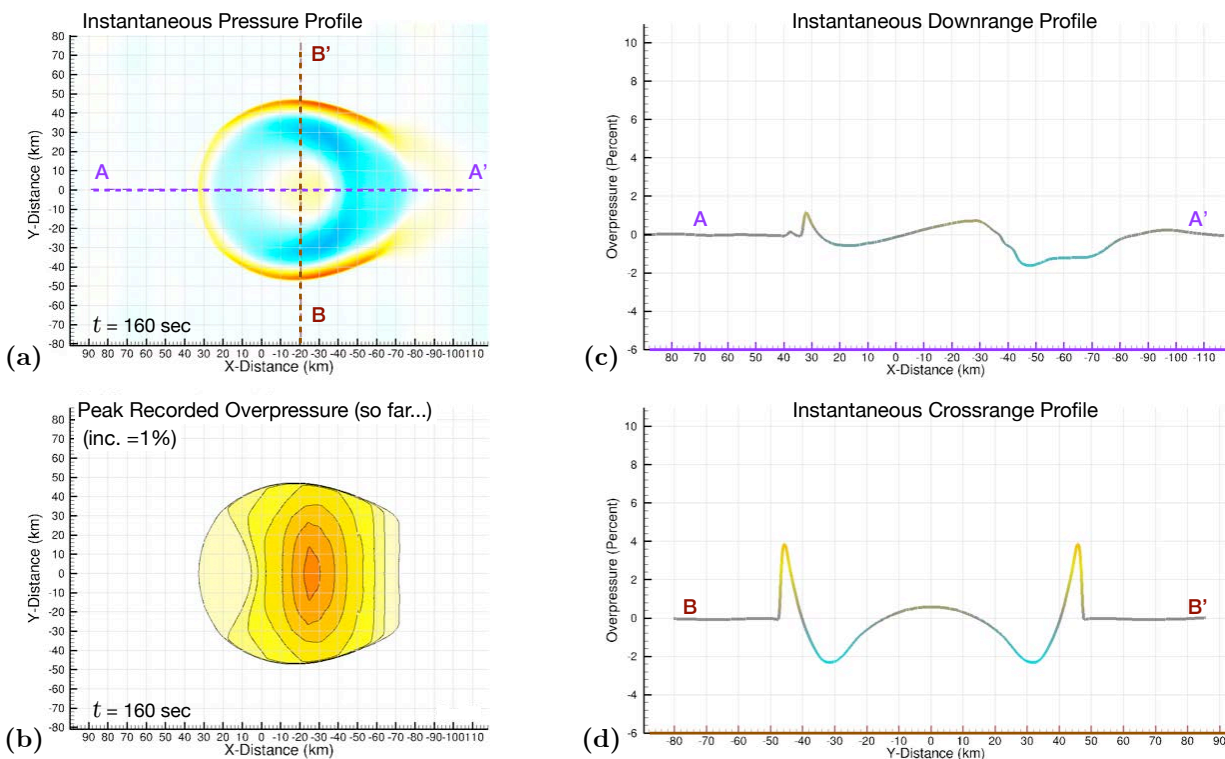


Figure 8. Evolution of ground footprint for Chelyabinsk meteor case at elapsed time of 160 sec. (a) Instantaneous ground overpressure (b) Peak ground overpressure, (c) Downrange plot of pressure directly under track along line AA' (d) Crossrange plot of pressure along line BB'.

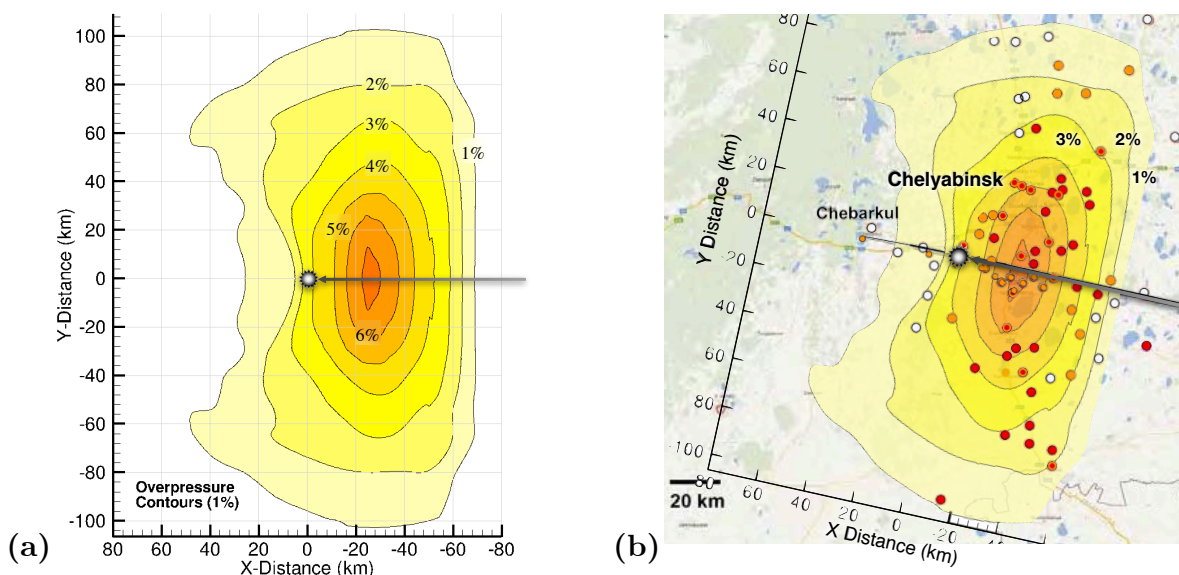
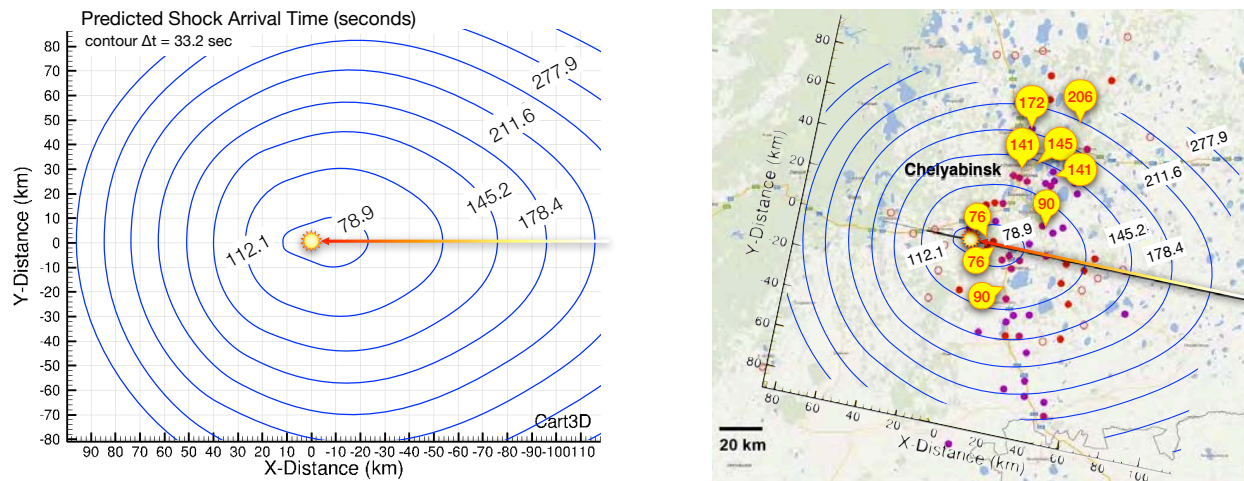


Figure 9. Ground footprint for Chelyabinsk meteor showing computed peak overpressures overlaid on ground-damage map<sup>1</sup> (right) using the energy deposition profile from Brown *et al.*<sup>3</sup> Increment between isobars is 1% of sea level pressure for standard atmosphere. Statistical correlations in Mannan and Lees<sup>34</sup> for blast-wave data indicate that an overpressure of ~700 Pa (0.69%) is able to shatter about 5% of typical glass windows while  $\Delta p$  of ~6% breaks roughly 90%.



**Figure 10. Ground footprint showing computed shock-wave arrival time at ground level in elapsed time from peak brightness. Map at right shows ground-track with the trajectory ending at (0,0). Placemarks on map show blast arrival times (in secs) collected by the Chelyabinsk Airburst Consortium.<sup>1,32</sup>**

predicted overpressure contours correlate well with the glass damage reports.<sup>1,32</sup>

The peak ground overpressure is around 7% and is located about 24 km prior to the end of the trajectory ( $x = -24$ ), directly under the flight path. The location of this peak is in excellent agreement with the most severe ground damage and injury reports. The highest fraction of the population that reported injuries was in the town of Korkino, which is located just 7 km from the peak predicted ground overpressure.<sup>1,32</sup> Simulations done with the SOVA hydrocode also predict a similar footprint and peak overpressure location.<sup>32</sup>

#### 4. Blast Arrival Times

Figure 10 shows predicted shock-wave arrival time at ground level for comparison to data in [1] and [32]. The time increment between successive contours is  $\Delta t = 33.2$  sec, and all times are reported with respect to peak brightness (4.2 sec elapsed time). The map in the right frame shows the ground track and, placemarks on the map show data collected by the Chelyabinsk Airburst Consortium. These data are considered quite reliable since many observations came from video recordings with time data synchronized through cell-service networks. The earliest arrival reported was 76 sec after peak brightness. The blast arrives at Korkino and Yemanzhelinsk approximately 90 sec after peak brightness and in the vicinity of Chelyabinsk at 140–145 sec after peak brightness. Although predictions from the simulation neglect local wind, temperature and other effects of the real atmosphere, they are all within seconds of the collected data and the best predictions in the literature.

#### 5. Computational Expense

In total, this simulation covered 5 min and 20 sec of real time. Over the final four minutes, the blast was in contact with the ground, and the footprint expanded to roughly 140 km from ground zero. Propagation of the airburst from the trajectory to the ground required  $\sim 80$  sec, and the entry itself was over within the first 6 secs. Despite accounting for under 2% of elapsed time, modeling of the entry consumed roughly 25% of the computational resources. This portion of the simulation used time steps of  $\sim 0.003$  sec, which were an order of magnitude smaller than those used while the blast propagated along the ground. With 90 M cells, the total simulation consumed required  $\sim 12$  hrs of wall-clock time using 1000 compute cores.<sup>d</sup> Considering the complexity of the physics and the level of fidelity, these are respectable numbers. Nevertheless, given our desire to perform parametric studies to examine sensitivities, it is clearly worth investigating simplifications to further reduce computational expense.

### C. Line-Source vs. Time-Dependent Entry Models

As evident from the discussion above, the vast difference between the time scales of the entry physics and subsequent propagation of the blast over the local terrain gives rise to substantial stiffness in the numerical

<sup>d</sup>2014 Xeon “Ivy Bridge” cores on NASA’s Pleiades computer.

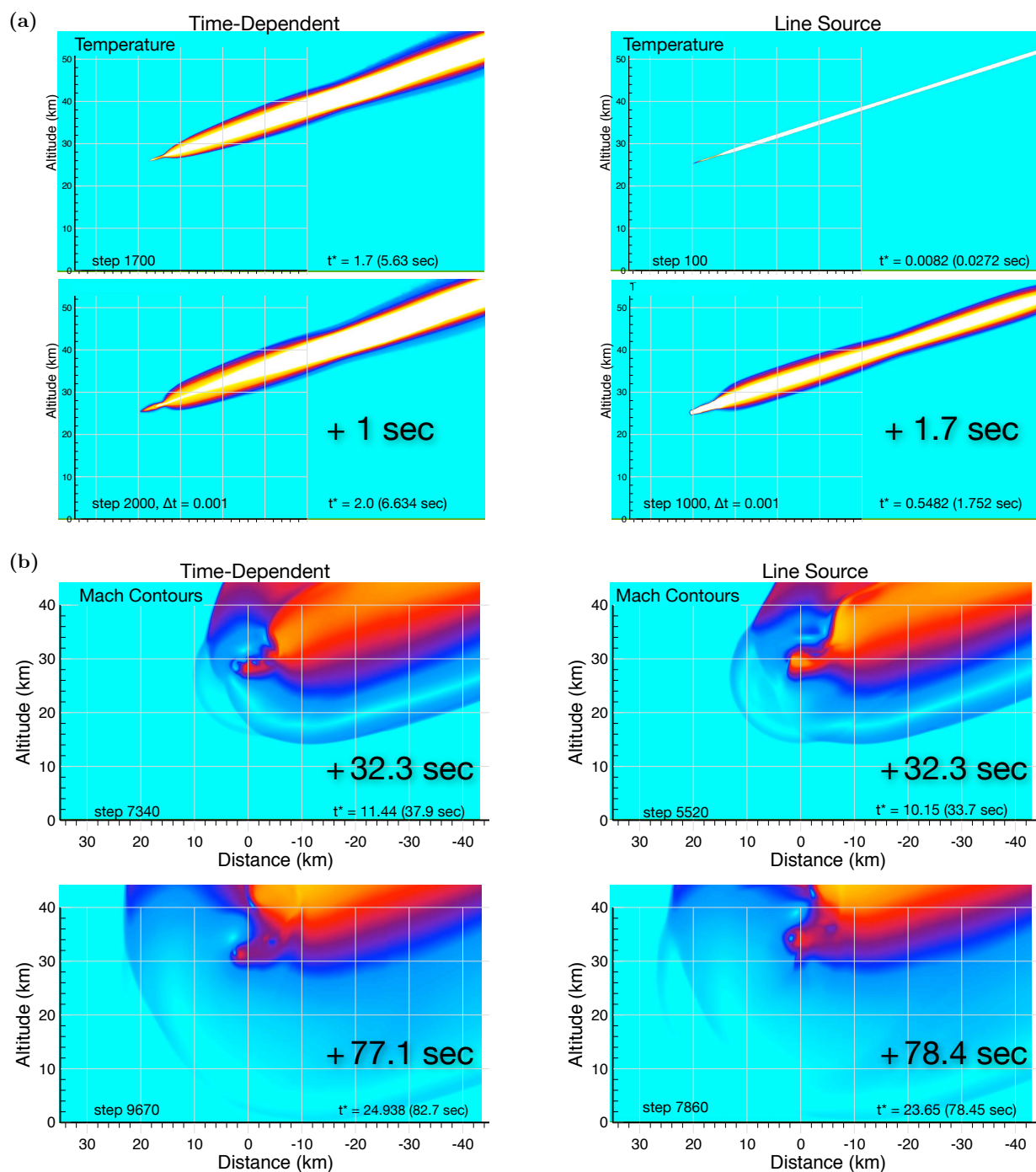
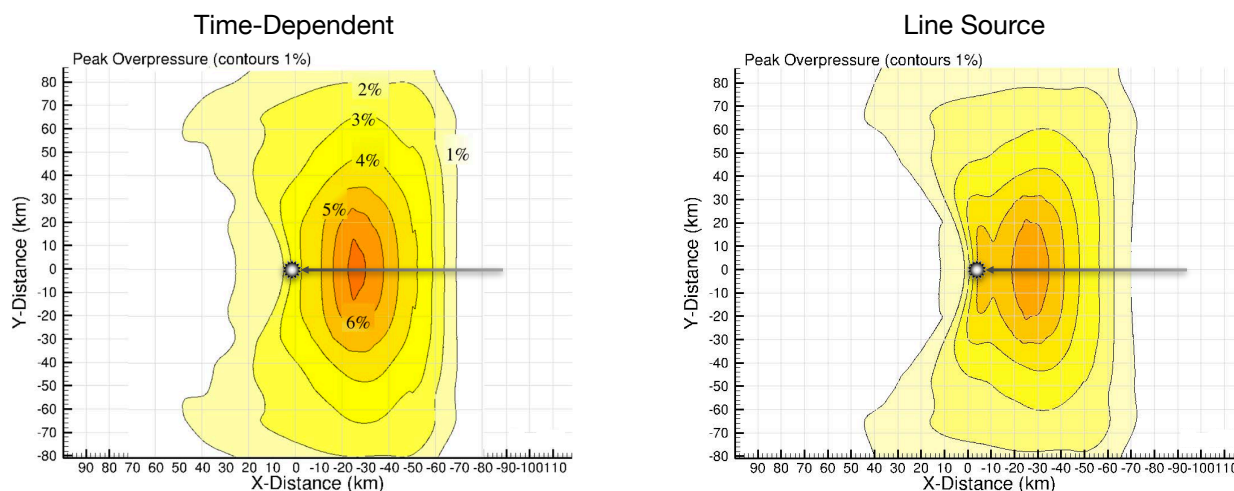


Figure 11. Comparison of entry and evolution using full time-dependent (left) and instantaneous line source (right) modeling. Frame (a) compares the evolution immediately after entry, while frame (b) shows the evolution after  $\sim 80$  seconds, near the time when the blast first arrives at the ground.





**Figure 12.** Comparison of peak ground overpressures using full time-dependent simulation (left) and instantaneous line source modeling (right).

simulation. The entry is over in seconds, while propagation lasts for minutes. One approach to reduce this disparity is to consider a line-source model of the entry, in which mass, momentum and energy are deposited instantaneously along the entire length of the entry trajectory. This approach is conceptually similar to the approach of ReVelle,<sup>12</sup> which is based upon the use of line-source blast waves assuming objects entering at “infinite” Mach number. In the current implementation, however, we use the conservation analysis in § II.C to properly include sources for mass and momentum deposition along the entry trajectory as well.

Figure 11 shows a comparison of entry and evolution using full time-dependent (left) and instantaneous line source (right) modeling. The upper two rows (frame a) show the evolution immediately after entry, while the lower two rows (frame b) display the evolution near the time when the blast first arrives at the ground (after ~80 seconds). The upper frame shows that in the first few seconds after entry, there is considerable discrepancy between the models, especially at higher altitudes. Since the initial propagation speed is extremely fast, the blast in the time-dependent simulation has expanded considerably (~5 km) further than in the line-source model. However, as the blast wave decelerates, the two approaches become increasingly similar. Snapshots in the lower frame show that a little more than 30 seconds later the extent of the blast is nearly identical between the two approaches. Measured from peak brightness, both blasts reach the ground within a second of each other and have largely similar structure and geometry.

Figure 12 shows a comparison of the ground footprint using full time-dependent entry with that of an instantaneous line source. The contours show peak predicted ground overpressure measured in percent of ambient pressure at sea level. While there are differences on the order of 1% at the earliest arrival times, these differences essentially vanish as the footprint evolves. As expected from the blast propagation overview in Figure 11, the overall shape of the footprints compare very well and the aspect ratio of the footprint (downrange vs. crossrange) are extremely similar. Importantly, the location of the peak ground overpressure is essentially identical in the two simulations and is directly under the trajectory, approximately 25 km before termination. Finally, note that the geometry of the blast shock structure dictates that low-angle trajectories (like this one at 18°) will show the most discrepancy between time-dependent and line-source entry models.

While the entry happens much faster than the blast propagation, the small time steps necessary to resolve the high entry speed mean that it consumes a disproportionate amount of the overall computational budget. After extensive simulations of numerous bolides, our general conclusion is that line-source modeling typically offers savings of about 25% of the computational budget. The model shows the best correlation with time-dependent entry modeling when the half-energy height is relatively high so that the blast has time to decelerate before hitting the ground. Ground overpressure footprints show the most discrepancy at lower trajectory angles. Shorter propagation times result in larger differences, while longer propagation and higher entry angles yield footprints that are in closer agreement.

## D. 90° Entry Angle

Risk assessment is generally performed using Monte Carlo simulations of static airbursts varying both the altitude and strength of the detonation.<sup>35,36</sup> This allows handbook methods to be used to predict ground damage through statistical correlation.<sup>9,18</sup> As we transition our risk assessment to include physics-based blast predictions, the 90° (vertical) entry case is of particular interest. Over flat terrain, symmetry dictates that at this entry angle, the blast footprint will consist of a series of concentric circles describing variation in overpressure with distance from ground-zero. Since the energy deposition profile is roughly logarithmic with altitude, the vast majority of the energy along the trajectory is released near the point of peak brightness. Given these observations, it's interesting to compare the ground overpressures from simulations from a 90° entry trajectory with those from a spherical detonation of the same magnitude at the same altitude. This case provides an important bridge between the detailed simulation of entry trajectories with more traditional static airburst correlations.

Figure 13 compares the blast evolution from a vertical (90°) line source for a Chelyabinsk-like deposition profile with that of a spherical charge of 1 km radius. To facilitate comparison with the earlier simulations, we set the half-energy height of the line source and the burst height of the spherical charge to 29.5 km.<sup>e</sup> Both simulations released a total of 520 kt of energy. Figure 13 presents the temporal evolution of both scenarios through several snapshots. The uppermost snapshots are taken shortly after energy release, at  $t^* = 3.14$ . At the left, buoyancy-driven vortical structures from the line source travel upward along the trajectory while the core continues to advance toward the ground. At the right, the spherical blast has propagated a radial distance of about 10 km from the blast center and the bubble has begun to flatten due to buoyancy effects acting upon the hot gas within. Despite these disparate initial conditions, marked similarities appear with advancing time. While the trajectory simulation retains a more intricate structure, it is clear from both the color map and the evolution of the blast front that the strength and speed of the shock advancing toward the ground are very similar in the two simulations. The final frames show the blast evolution at  $t^* = 35.5$  (~114secs) after detonation. Both blasts have reached the ground plane, and the ground footprint has expanded to a radius of ~30 km from ground-zero in both simulations.

Figure 14 shows a detailed comparison of the overpressure envelope on the ground. For reference, the frame at the left shows a vertical slice through the domain (via overpressure contours,  $(p - p_\infty)/p_\infty$ ) taken at around 139 seconds after energy release. The right frame shows the envelope of recorded over/underpressure as well as instantaneous pressure profiles for both scenarios at 139 sec. The yellow-shaded region shows the envelope for the spherical charge while the red line shows that of the line-source. Away from ground-zero, the envelopes for the two cases are remarkably similar. In particular, the decay of the envelope with radius increasing as far out as 100 km is very well predicted by the spherical approximation. Nearer to the origin, the spherical charge over-predicts the line source. This appears to be related to the weak final fragmentation event near the end of the trajectory in this particular deposition profile. This event is visible in both the energy and mass deposition profiles in Figure 5. Its consequences are evident in the top three frames of the blast from the line source in Figure 13, where it weakens the main blast front as it advances toward the ground near the origin. Since the spherical charge was initially homogeneous, it contains no such structures.

The instantaneous pressure profiles shown by the red and blue dashed lines in the frame at the right of Figure 14 show remarkable similarities. At 139 seconds, both have expanded to a radius of just over 40 km. The instantaneous pressure profiles (red and blue dashed lines) have essentially identical peak values as well as the same integrated impulse.

## IV. Summary and Future Work

Meteoroids enter the atmosphere at astronomical speeds and their deceleration and heating transfers mass, momentum and energy into the surrounding air at tremendous rates. Blast waves resulting from this trauma can propagate hundreds of kilometers and cause substantial terrestrial damage even when no ground impact occurs. This work is part of a larger effort within NASA to better quantify the threat posed by these objects. This paper presented a new simulation technique for bolide-entry modeling that can be used to parametrically drive simulation-based assessment of these risks.

The technique uses profiles of the energy deposited into the atmosphere as input. These profiles can come from analytic or statistical models, numerical methods, hydrocode simulations or from actual observation of

<sup>e</sup>In reality, a vertical entry would typically have a lower burst height, other factors being equal.

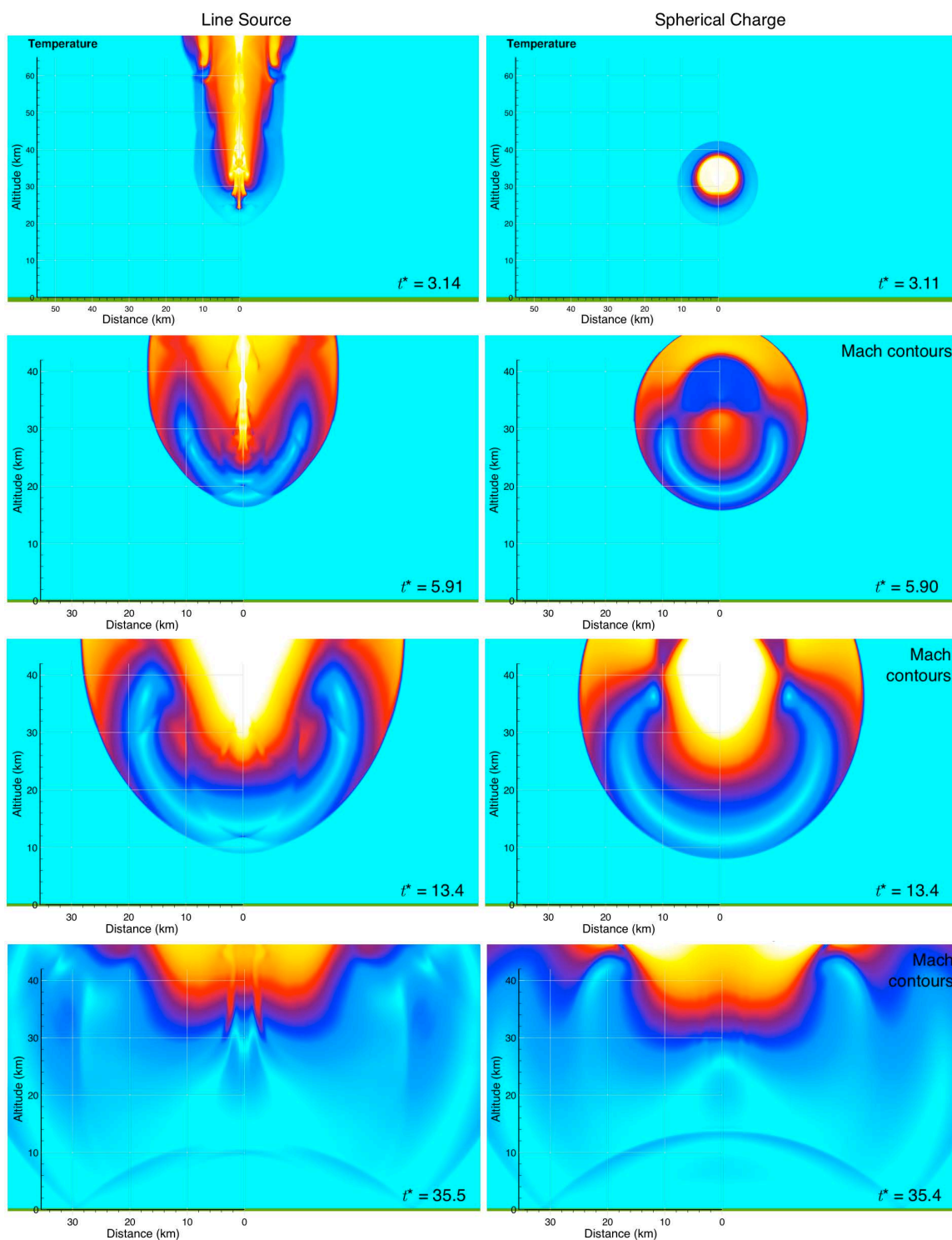
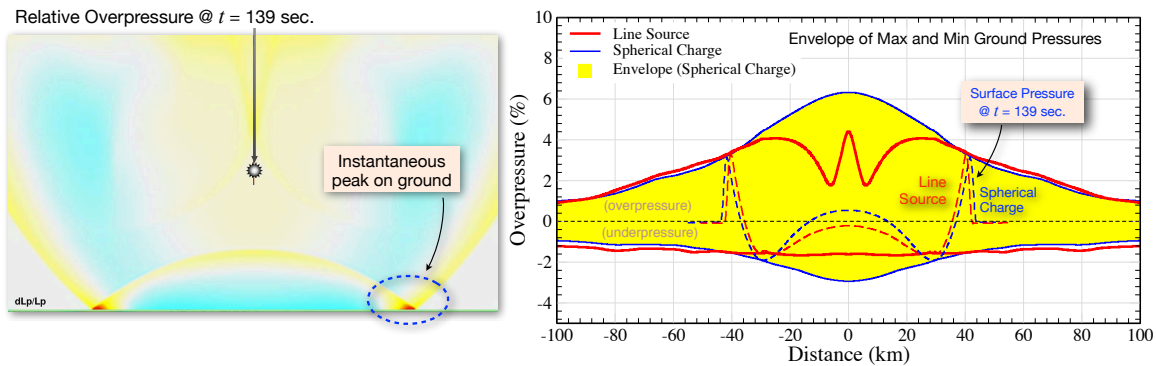


Figure 13. Comparison of blast evolution from a line source for a Chelyabinsk-like deposition profile with that of a spherical charge of 1 km radius for a 90° entry. Burst height = 29.5 km, Total energy = 520 kt. Time (sec) =  $t^* \times 3.21$ .





**Figure 14.** Comparison of overpressure envelope from a vertical entry ( $90^\circ$ ) line source with a Chelyabinsk-like deposition profile with that of a spherical charge with a 1 km radius. Burst height = 29.5 km, Total energy = 520 kt. Dashed lines show instantaneous ground pressure profiles for both simulations at 139 sec after energy release.

particular events. We showed how, when combined with trajectory information, conservation analysis can be used with these profiles to derive time-dependent sources that conserve mass, momentum and energy of the entire system. These source terms drive 3-D simulations of bolide-entry using a fully-conservative, finite-volume method on multilevel Cartesian meshes. These simulations typically cover several hundred thousand square kilometers of terrain and predict the blast arrival time, overpressure data, wind speeds and other data resulting from the airburst.

We presented numerical results that ranged from simple verification exercises using a uniform spherical charge to a detailed reconstruction of the 2013 Chelyabinsk meteor entry over Russia. For this latter case, the method predicted a ground footprint that was in excellent agreement with data collected by the Chelyabinsk Airburst Consortium.<sup>1,32</sup> Predicted overpressures showed strong agreement with glass-breakage data covering a region of over 20,000 km<sup>2</sup> using standard statistical correlations. The predicted peak ground pressures were ~7 km from the town of Korkino, which reported the highest fraction of injuries per-capita. The earliest reported blast arrival was 76 sec after peak brightness, and predictions in the vicinity of Chelyabinsk were around 141-145 secs. Predicted blast arrival times agree with observations throughout the simulation domain to within seconds.

The investigations examined various approximations to the entry physics aimed at decreasing the computational expense while still retaining sufficient fidelity to drive the ground damage estimates required for credible risk assessment. Using a line-source or spherical charge model for the entry reduced the simulation time by about 25%. For the Chelyabinsk case, line-source modeling of the entry predicted local ground overpressures within ~1% of the complete time-dependent entry model. Blast arrival times were similarly good. Nevertheless, we noted that the geometry of the blast dictates that greater discrepancies would be expected for cases with lower effective airburst altitudes — especially when combined with low entry angles.

Moving forward, there are several near-term roles for this work. One specific area of persistent concern is the potential for large airbursts over water to trigger tsunamis which can impact much larger regions of the globe.<sup>18,37-39</sup> Coupling our airburst simulation capability with tsunami modeling efforts is an immediate priority. By parametrically driving entry characteristics like speed, strength and size, seek to develop a broader understanding of the key parameters that determine the ground footprint. This knowledge will support simulation-based risk assessment to enable statistical quantification of the asteroid threat. In addition to contributing to these larger efforts, the simulation capability described here also offers a nascent capability for rapid-response modeling of specific potentially hazardous objects that may be identified by sky surveys.<sup>40</sup>

## Acknowledgments

The authors wish to thank Darrel Robertson, Lorian Wheeler and other members of the NASA Asteroid Threat Assessment Project for their superb effort, insight and support throughout this work. This research was supported by the Near-Earth Object program within the NASA Science Mission Directorate's Planetary Sciences Division. Marian Nemec was supported under NASA Ames Research Center Contract NNA10DF26C. Computer support was provided by the NASA Advanced Supercomputing facility at NASA Ames.

## References

- <sup>1</sup>Popova, O. P., Jenniskens, P., Emel'yanenko, V., Kartashova, A., and Biryukov, E., *et al.*, "Chelyabinsk Airburst, Damage Assessment, Meteorite Recovery, and Characterization," *Science*, Vol. 342, No. 6162, 2013, pp. 1069–1073, <http://dx.doi.org/10.1126/science.1242642>.
- <sup>2</sup>National Aeronautics and Space Administration Office of Space Science, "Bolide Events 1994–2013," <http://neo.jpl.nasa.gov/news/news186.html>, 2013.
- <sup>3</sup>Brown, P. G., Assink, J. D., Astiz, L., Blaauw, R., and Boslough, M. B., *et al.*, "A 500-kiloton airburst over Chelyabinsk and an enhanced hazard from small impactors," *Nature*, Vol. 503, No. 6162, November 2013, pp. 238–241, <http://dx.doi.org/10.1038/nature12741>.
- <sup>4</sup>Stokes, G. H., Yeomans, D. K., Bottke, W. F., Jewitt, D., and Chesley, S. R., *et al.*, "Study to Determine the Feasibility of Extending the Search for Near-Earth Objects to Smaller Limiting Diameters," *National Aeronautics and Space Administration Office of Space Science*, August 2003, <http://neo.jpl.nasa.gov/neo/neoreport030825.pdf>.
- <sup>5</sup>Arnold, J. O., *et al.*, "NASA Ames Planetary Defense Integrated Product Team: An Overview," *Proceedings of the 12th International Planetary Probe Workshop*, Cologne, Germany, June 2015.
- <sup>6</sup>Shuvalov, V. and Artemieva, N., "Numerical modeling of Tunguska-like impacts," *Planetary and Space Science*, Vol. 50, No. 2, February 2002, pp. 181–192, [http://dx.doi.org/10.1016/S0032-0633\(01\)00079-4](http://dx.doi.org/10.1016/S0032-0633(01)00079-4).
- <sup>7</sup>ReVelle, D. O., "NEO fireball diversity: energetics-based entry modeling and analysis techniques," *Near Earth Objects, our Celestial Neighbors: Opportunity and Risk*, Vol. 2 of *Proceedings of the International Astronomical Union*, 8 2006, pp. 95–106.
- <sup>8</sup>Korobeinikov, V., Gusev, S., Chushkin, P., and Shurshalov, L., "Flight and fracture of the Tunguska cosmic body into the Earth's atmosphere," *Comput. & Fluids*, Vol. 21, No. 3, 1992, pp. 323 – 330, [http://dx.doi.org/10.1016/0045-7930\(92\)90041-S](http://dx.doi.org/10.1016/0045-7930(92)90041-S).
- <sup>9</sup>Samuel Glasstone and Philip J. Dolan, *The Effects of Nuclear Weapons*, United States Department of Defense and the Energy Research and Development Administration, 3rd ed., 1977, <http://www.fourmilab.ch/etexts/www/effects/>.
- <sup>10</sup>Boslough, M. B. E. and Crawford, D., "Low-Altitude Airbursts and the Impact Threat," *International Journal of Impact Engineering*, Vol. 35, No. 12, 2008, <http://dx.doi.org/10.1016/j.ijimpeng.2008.07.053>.
- <sup>11</sup>Boslough, M. B. E., "Airburst Warning and Response," *Acta Astronautica*, Vol. 103, October–November 2014, pp. 370–375, <http://dx.doi.org/10.1016/j.actaastro.2013.09.007>.
- <sup>12</sup>ReVelle, D. O., "On Meteor-Generated Infrasound," *Journal of Geophysical Research*, Vol. 81, No. 7, March 1976, pp. 1217–1230.
- <sup>13</sup>ReVelle, D., "Recent Advances in Bolide Entry Modeling: A Bolide Potpourri," *Earth, Moon, and Planets*, Vol. 97, No. 1–2, 2005, pp. 1–35, [10.1007/s11038-005-2876-4](http://dx.doi.org/10.1007/s11038-005-2876-4).
- <sup>14</sup>Cepplecha, Z. and ReVelle, D. O., "Fragmentation model of meteoroid motion, mass loss, and radiation in the atmosphere," *Meteoritics & Planetary Science*, Vol. 40, No. 1, 2005, pp. 35–54, <http://dx.doi.org/10.1111/j.1945-5100.2005.tb00363.x>.
- <sup>15</sup>Hills, J. G. and Goda, P. M., "The Fragmentation of Small Asteroids in the Atmosphere," *The Astronomical Journal*, Vol. 105, No. 3, March 1993, pp. 1114–1144.
- <sup>16</sup>Internat. Org. for Standardization and U. S. Environmental Protection Agency, *Standard Atmosphere: ISO 2533:1975*, International Organization for Standardization, December 1978.
- <sup>17</sup>Mathias, D. L., Wheeler, L., Prabhu, D., Aftosmis, M. J., Dotson, J., and Robertson, D., "Sensitivity to Uncertainty in Asteroid Impact Risk Assessment," American Geophysical Union, December 2015.
- <sup>18</sup>Collins, G. S., Melosh, H. J., and Marcus, R. A., "Earth Impact Effects Program: A Web-based computer program for calculating the regional environmental consequences of a meteoroid impact on Earth," *Meteoritics & Planetary Science*, Vol. 40, No. 6, June 2005, pp. 817–840, <http://dx.doi.org/10.1111/j.1945-5100.2005.tb00157.x>.
- <sup>19</sup>Cepplecha, Z., Borovička, J., and Spurný, P., "Dynamical behavior of meteoroids in the atmosphere derived from very precise photographic records," *Astronomy & Astrophysics*, Vol. 357, May 2000, pp. 1115–1122.
- <sup>20</sup>Aftosmis, M. J., Berger, M. J., and Melton, J. E., "Robust and Efficient Cartesian Mesh Generation for Component-Based Geometry," *AIAA Journal*, Vol. 36, No. 6, June 1998, pp. 952–960.
- <sup>21</sup>van Leer, B., "Flux-Vector Splitting for the Euler Equations," ICASE Report 82-30, Sept. 1982.
- <sup>22</sup>Berger, M. J., Aftosmis, M. J., and Murman, S. M., "Analysis of Slope Limiters on Irregular Grids," *AIAA Paper 2005-0490*, Jan. 2005.
- <sup>23</sup>Antony Jameson, "Time Dependent Calculations Using Multigrid, with Applications to Unsteady Flows Past Airfoils and Wings," *AIAA Paper 1991-1596*, 1991.
- <sup>24</sup>Melson, N. D., Sanetrik, M. D., and Atkins, H. L., "Time-accurate Navier-Stokes Calculations with Multigrid Acceleration," *Proceedings of the 6th Copper Mountain Conference on Multigrid Methods*, Copper Mountain, Colorado, April 1993.

- <sup>25</sup>Mavriplis, D. J., Aftosmis, M. J., and Berger, M. J., "High resolution aerospace applications using the NASA Columbia supercomputer," *International Journal of High Performance Computing Applications*, Vol. 21, No. 1, January 2007, pp. 106–126.
- <sup>26</sup>Aftosmis, M. J., "Cart3D → Main Page <http://people.nas.nasa.gov/aftosmis/cart3d/>," 2015.
- <sup>27</sup>Brode, H. L., "Blast Wave from a Spherical Charge," *Physics of Fluids*, Vol. 2, No. 2, 1959, pp. 217–229.
- <sup>28</sup>Jones, D. L., "Intermediate Strength Blast Wave," *Physics of Fluids*, Vol. 11, No. 8, 1968, pp. 1664–1667.
- <sup>29</sup>Taylor, G. I., "The formation of a blast wave by a very intense explosion: I. Theoretical discussion," *Proc. Roy. Soc. London*, Vol. A201, No. 1065, 1950, pp. 159–174.
- <sup>30</sup>von Neumann, J., "The point source solution," U.S. Government Document AM-9, National Defense Research Council, Division B, Washington, DC, USA, June 1941.
- <sup>31</sup>Antanovskii, L., "Solving multi-dimensional problems of gas dynamics using MATLAB," Technical Report DSTO-TR2139, Defence Science and Technology Organisation (Australia), June 2008.
- <sup>32</sup>Popova, O. P., Shuvalov, V., Jenniskens, P., Svetsov, V., Glazachev, D., and Rybnov, Y., "Simulations of the entry and damaging effects of asteroid impacts," *First International Workshop on Potentially Hazardous Asteroids Characterization, Atmospheric Entry and Risk Assessment*, NASA Ames Research Center, (Presentation only) <https://planetary-defense.arc.nasa.gov/workshop2015/>, July 2015.
- <sup>33</sup>de Groot-Hedlin, C. D. and Hedlin, M. A., "Infrasound detection of the Chelyabinsk meteor at the USArray," *Earth and Planetary Science Letters*, Vol. 402, 2014, pp. 337 – 345.
- <sup>34</sup>Mannan, M. S. and Lees, F. P., *Lees' Loss Prevention in the Process Industries (Third Edition)*, Butterworth-Heinemann, Burlington, third edition ed., 2005.
- <sup>35</sup>Motiwalla, S. A., Mathias, D. L., and Mattenberger, C. J., "An Integrated Physics-based Risk Model for Assessing the Asteroid Threat," No. 12351, International Topical Meeting on Probabilistic Safety Assessment and Analysis, Sun Valley, ID, USA, 2015.
- <sup>36</sup>Mathias, D. L., Robertson, D. K., and Aftosmis, M. J., "Sensitivity of Ground Damage Prediction to Meteoroid Breakup Modeling Assumptions," *4th IAAA Planetary Defense Conference (PDC 2015)*, 2015.
- <sup>37</sup>Berger, M. J., "Simulation of Air-Burst Generated Tsunamis Using GeoClaw," *First International Workshop on Potentially Hazardous Asteroids Characterization, Atmospheric Entry and Risk Assessment*, NASA Ames Research Center, (Presentation only) <https://planetary-defense.arc.nasa.gov/workshop2015/>, July 2015.
- <sup>38</sup>Ezedine, S., Miller, P. L., and Dearborn, D. S. P., "Wave Generation, Wave Propagation and Consequences of Asteroid Impacts on Earth," *First International Workshop on Potentially Hazardous Asteroids Characterization, Atmospheric Entry and Risk Assessment*, NASA Ames Research Center, (Presentation only) <https://planetary-defense.arc.nasa.gov/workshop2015/>, July 2015.
- <sup>39</sup>Gisler, G. R., Ferguson, J. M., Plesko, C. S., and Weaver, R. P., "Airburst vs Impact: Which Makes the Greater Wave?" *First International Workshop on Potentially Hazardous Asteroids Characterization, Atmospheric Entry and Risk Assessment*, NASA Ames Research Center, (Presentation only) <https://planetary-defense.arc.nasa.gov/workshop2015/>, July 2015.
- <sup>40</sup>Milani, A., Chesley, S. R., Chodas, P. W., and Valsecchi, G. B., "Asteroid Close Approaches: Analysis and Potential Impact Detection," *Asteroids III*, edited by W. Bottke, A. Cellino, P. Paolicchi, and R. Binzel, No. University of Arizona Press, <http://www.lpi.usra.edu/books/AsteroidsIII/pdf/3040.pdf>, 2002.